Dalton Transactions

PAPER

View Article Online
View Journal | View Issue

Cite this: *Dalton Trans.*, 2016, **45**, 7847

Further insights into the chemistry of the Bi–U–O system

Karin Popa,*[a] Damien Prieur,[a] Dario Manara,[a] Mohamed Naji,[a] Jean-François Vigier,[a] Philippe M. Martin,[b] Oliver Dieste Blanco,[a] Andreas C. Scheinost,[c] Tim Prüßmann,[d] Tonya Vitova,[d] Philippe E. Raison,[a] Joseph Somers[a] and Rudy J. M. Konings[a]

Received 24th February 2016,
Accepted 5th April 2016

DOI: 10.1039/c6dt00735j

www.rsc.org/dalton

Cubic fluorite-type phases have been reported in the $U^{IV}O_2$–Bi_2O_3 system for the entire compositional range, but an unusual non-linear variation of the lattice parameter with uranium substitution has been observed. In the current extensive investigation of the uranium(IV) oxide–bismuth(III) oxide system, this behaviour of the lattice parameter evolution with composition has been confirmed and its origin identified. Even under inert atmosphere at 800 °C, U^{IV} oxidises to U^{V}/U^{VI} as a function of the substitution degree. Thus, using a combination of three methods (XRD, XANES and Raman) we have identified the formation of the $BiU^{V}O_4$ and $Bi_2U^{VI}O_6$ compounds, within this series. Moreover, we present here the Rietveld refinement of $BiU^{V}O_4$ at room temperature and we report the thermal expansion of both $BiU^{V}O_4$ and $Bi_2U^{VI}O_6$ compounds.

Introduction

The Bi–U–O ternary system came to our attention in the frame of the safety assessment of lead bismuth eutectic (LBE) cooled fast reactors. The LBE cooled fast reactors concept is one of the systems being developed in Europe within the European Sustainable Nuclear Industrial Initiative (ESNII) and is the coolant of choice for the MYRRHA reactor project in Belgium.[1] Thus, the phase relations in the Pb–Bi–U–Pu–O system should be studied in detail, in order to identify possible phases that could be formed during inadvertent fuel (MOX) – coolant (LBE) interactions.[2]

Very few compounds have been identified in the Bi–U–O ternary system to date. Bismuth(III) monouranate, $Bi_2U^{VI}O_6$, is the only compound well characterized from a crystallographic point of view and has been prepared by several high- and low-temperature procedures.[3–7] It was reported to exist in two closely related crystalline modifications. The room temperature form, α-Bi_2UO_6 (space group $C2$)[8] undergoes a phase transition above 600 °C into the β-form ($P\bar{3}$ space group).[8,9] For this compound, the heat capacity was measured and a number of thermodynamic functions have been reported recently.[10]

$BiU^{V}O_4$ has been prepared and reported to have a defect fluorite structure ($Fm\bar{3}m$) at room temperature.[11,12] The pentavalent oxidation state of uranium was deduced from the co-proportionation reaction between stoichiometric amounts of UO_2, U_3O_8, and Bi_2O_3. Further magnetic susceptibility measurements indicated a paramagnetic behaviour,[13] consistent with the pentavalent oxidation state of uranium. However, no Rietveld refinement has been published for this compound to date.

Cubic fluorite-type phases have been reported in the system $U^{IV}O_2$–Bi_2O_3 for the entire compositional range by Hund.[14] The non-linear variation of the lattice parameters observed in this study was explained based on the fact that the substitution increases the amount of anionic vacancies with increasing Bi_2O_3 content. However, this explanation assumes that the uranium remains in oxidation state IV in the synthesised powders. Thus, we initiated a comprehensive study on the oxidation states in the Bi–U–O system, focused on both uranium and bismuth. We present here the solid state synthesis of different compositions in the Bi–U–O system, the formation of the $BiU^{V}O_4$ and $Bi_2U^{VI}O_6$ compounds in the reaction conditions, the Rietveld refinement of the $BiU^{V}O_4$ and the thermal expansion of $BiU^{V}O_4$ and $Bi_2U^{VI}O_6$.

Materials and methods

Synthetic procedures

The uranium(IV) oxide–bismuth(III) oxide solid solutions were produced using the solid state reaction procedure previously reported (Hund).[14] Thus, stoichiometric amounts of commer-

[a]*European Commission, Joint Research Centre, Institute for Transuranium Elements, P.O. Box 2340, D-76125 Karlsruhe, Germany. E-mail: karin.popa@ec.europa.eu*
[b]*CEA, DEN, DEC/SESC, F-13108 Saint Paul Lez Durance Cedex, France*
[c]*Helmholtz-Zentrum Dresden-Rossendorf, Institute of Resource Ecology, D-01314 Dresden, Germany*
[d]*Forschungszentrum Karlsruhe/K.I.T., Institute for Synchrotron Radiation – ANKA, Germany*

cial α-bismuth(III) oxide (Sigma-Aldrich, 99.999% trace metal basis) and $UO_{2.10}$ (COGEMA powder, stoichiometry calculated form the value of the lattice parameter) were reacted for 48 h at 800 °C under an argon atmosphere (with an oxygen content of 7 ppm) in specifically designed hermetically closed glove-boxes for handling radioactive materials. Note that the non-stoichiometric uranium oxide was chosen in this experiment in order to reproduce the working conditions presented by Hund.[14] However, the composition having the ratio Bi : U = 1 : 1 and 2 : 1 were also produced starting from fully stoichiometric $UO_{2.00}$ under the same reaction conditions.

The α-Bi_2UO_6 used for HT-XRD experiments was prepared by conventional solid state reaction (5 h of at 800 °C under air) of commercial α-bismuth(III) oxide with a stoichiometric amount of amorphous uranium(VI) oxide.

X-ray powder diffraction

α-Bi_2UO_6 was characterised at room temperature by X-ray powder diffraction (XRD) using a Bruker D8 diffractometer mounted in a Bragg-Brentano configuration with a curved Ge (111) monochromator, a ceramic copper tube (40 kV, 40 mA) equipped with a LinxEye position sensitive detector. The data were collected by step scanning in the angle range $10° \leq 2\theta \leq 120°$ at a 2θ step size of 0.0092°. For the measurement, the powder was deposited on a silicon wafer to minimize the background and dispersed on the surface with several drops of isopropanol. The structural refinement was performed using the Fullprof2k suite. The shape of the peaks was described by a Pseudo-Voigt function and the background was fitted based on linear interpolation between a set of about 50 background points. The scattering factors of all elements were used.

The thermal expansion of $BiUO_4$ and α-Bi_2UO_6 was followed by high-temperature X-ray diffraction experiments. The data were collected on a second Bruker D8 X-ray diffractometer mounted with a curved Ge (111) monochromator, a copper ceramic X-ray tube (40 kV, 40 mA), a LinxEye position sensitive detector and equipped with an Anton Paar HTK 2000 chamber. Measurements were conducted up to 600–700 °C under argon, in the angle range $16° \leq 2\theta \leq 90°$ with a 2θ step size of 0.017°.

HR-XANES spectroscopy

Uranium M_{IV} edge. The U M_{IV} (3728 eV) high energy resolution XANES (HR-XANES) spectra were recorded at the KIT INE-Beamline for actinide research at the ANKA synchrotron radiation facility (Karlsruhe, Germany) on 5 mg of powdered samples mixed with 20 mg of BN. The HR-XANES spectra have been collected using an Johann type multi-analyser X-ray emission spectrometer (MAC-Spectrometer).[15–17] The incident X-ray beam was monochromatized by a Si(111) double crystal monochromator (DCM) and focused to 500 × 500 μm onto the sample. The MAC-Spectrometer comprised five spherically bent Si(220) analyser crystals with 1 m bending radius and a single diode silicon drift detector (KETEK VIRUS SDD). These two components and the sample were arranged in a vertical Rowland circle geometry and placed in a glove box filled with helium. Continuous helium flow has maintained a constant 0.1% O_2 content in the box during the experiments. The DCM was calibrated by setting 3724.5 eV to the maximum of the most intense absorption resonance (white line, WL) of a HR-XANES spectrum pf a UO_2 reference compound. A short HR-XANES spectrum and a normal U M_β (~3337 eV) emission lines of this reference were measured after each sample. Normal emission lines were also measured before the HR-XANES spectra for each sample in order to monitor the stability of the spectrometer. The U M_{IV} HR-XANES spectra were obtained by recording the intensity of the U M_β emission line as a function of energy of the incident X-ray beam. The HR-XANES method is also often designated as high energy resolution fluorescence detected XANES (HERFD-XANES) or partial fluorescence yield XANES (PFY-XANES). The presented spectra have been normalized according to the maximum of the white line using the ATHENA software.[18] This method provides unique qualitative informations about the oxidation states present in the systems. The spectra of $(U^{IV},U^{V})_4O_9$ and $(U^{V},U^{VI})_3O_8$ were collected earlier on the ID26 beamline of the ESRF synchrotron.[19,20] The experimental energy resolution at the INE-Beamline and the ID26 beamline are about 1.3 eV and 0.9 eV, respectively. Bismuth and Uranium L_{III} edge.

XANES data were recorded at the European Synchrotron Radiation Facility (ESRF, France). 5 mg of powdered sample were mixed with boron nitride (BN) and pressed into pellets for XANES measurements. The storage ring operating conditions were 6.0 GeV and 160–200 mA. The XANES spectra were recorded at room temperature in transmission mode at the ROBL beamline dedicated to actinide elements.[21] A double crystal monochromator mounted with a Si (111) crystal was used. The energy calibration was achieved using platinum (Pt L_{II} edge: 13 273 eV) and yttrium (Y K edge: 17 038 eV) foil inserted between the second and third ionization chambers. For each XANES measurement, the spectra of the reference foil were systematically collected at the same time. Background subtraction and normalization have been achieved with ATHENA. To determine the oxidation states of bismuth, XANES spectra edges were compared to those of reference samples, *i.e.* $Bi_2^{III}O_3$, $Bi_2^{III}UO_6$ and $NaBi^{V}O_3{\cdot}xH_2O$, that were collected during the same experimental campaign. The oxidation state of uranium, was determined by comparing the absorption edges of the U L_{III} XANES spectra to those of spectra of reference samples, *i.e.* $U^{IV}O_2$, $(U^{IV},U^{V})_4O_9$, $(U^{V},U^{VI})_3O_8$ and $U^{VI}O_3$. Oxidation states were derived using a linear combination fitting (LCF) of these normalized reference spectra.

Raman spectroscopy

Raman spectra were measured with a Jobin–Yvon® T64000 spectrometer used in the single spectrograph configuration. The excitation source was a Kr^+ Coherent® continuous wave laser radiating at 647 nm, with a controllable nominal power, usually set to 100 mW at the exit of the cavity. The power impinging the sample surface was lower by approximately a factor 5. Spectra were measured in a confocal microscope with a 50-fold magnification and long focal distance (1 cm). This feature permits a good spectral resolution (±2 cm^{-1}) indepen-

dently of the surface shape, with a spatial resolution of 2 μm × 2 μm on the sample surface. The spectrograph angle was calibrated with the T_{2g} excitation of a silicon single crystal, set at 520.5 cm^{-1}.[22] The instrument is calibrated on a daily basis prior to measurement. Typical integration times ranged from 20 to 45 seconds with 3 cycles.

Scanning electron microscopy

A Philips XL40 Scanning Electron Microscope equipped with Energy Dispersive X-ray Spectroscopy (EDS) was used. The sample grains were deposited on the usual carbon sticker and covered with Carbon to avoid charging. Each sample was observed at different magnifications and EDS analysis performed to confirm its homogeneity, comparing the elemental composition on the general view with those from smaller regions.

Results and discussion

Elucidation of the non-linear behaviour of the lattice parameters in the uranium oxide–bismuth(III) oxide solid solution

Compositional characterisation. The relative chemical composition of the obtained Bi–U–O samples, as determined by SEM-EDS, is: (1) $Bi_{0.15}U_{0.85}O_{2.00}$; (2) $Bi_{0.25}U_{0.75}O_{2.00}$; (3) $Bi_{0.32}U_{0.68}O_{2.00}$; (4) $Bi_{0.40}U_{0.60}O_{2.00}$; (5) $Bi_{0.50}U_{0.50}O_{2.00}$; (6) $Bi_{0.60}U_{0.40}O_{1.95}$; (7) $Bi_{0.67}U_{0.33}O_{2.00}$; (8) $Bi_{0.79}U_{0.21}O_{1.81}$; and (9) $Bi_{0.85}U_{0.15}O_{1.70}$. The oxygen content was established based on the relative ionic metal composition (as determined by SEM-EDS) and their oxidation states (determined by XANES) as will be explained below (for the samples (1), (3), (5), (6), (7), and (8) – direct measurements, while for the samples (2), (4), and (9) – extrapolated).

XRD study. As already mentioned, cubic fluorite-type phases have been reported in the U^{IV} system, UO_2–Bi_2O_3, over the entire compositional range by Hund.[14] A non-linear variation of the lattice parameter has been observed, which was explained by the increase of anionic vacancies with increasing Bi_2O_3 content, assuming uranium remained at the oxidation state IV (Hund).[14] In the current investigation of the Bi–U–O system, we have confirmed this specific variation of the lattice parameter with composition, as shown in Fig. 1 and Table 1, suggesting that similar phases as Hund have been obtained.[14] It can be observed that the samples rich in uranium follow a quasilinear trend up to Bi : U = 1 : 1.

In almost all the compositions, syntheses lead to the formation of well crystalline Bi–U–O solid solutions with a fluorite structure (inset Fig. 1). As this structural description comes from diffraction data, it only describes an "average" of the atomic organisation on a long distance. Being a solid-solution of uranium and bismuth, there is a shared crystallographic position of the cations, *i.e.* a random distribution of the two elements in space.

Only $Bi_{0.67}U_{0.33}O_{2.00}$ crystallises in a specific structure with a monoclinic space group. As illustrated in Fig. 2, the former structure is strongly fluorite related. For this reason, despite

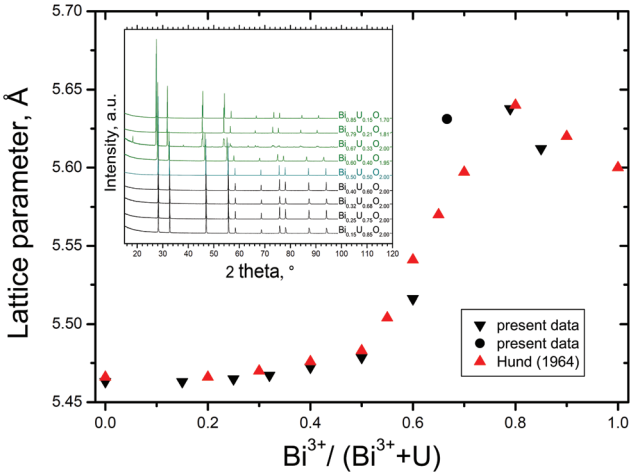

Fig. 1 Lattice parameter variation in the Bi–U–O system as a function of the substitution degree. For $Bi_{0.67}U_{0.33}O_{2.00}$ (●), see discussions. Inset: XRD patterns of the different mixed oxides analysed in this study.

Table 1 Lattice parameters for the Bi–U–O compositions

Chemical composition[a]	*a*, Å	*b*, Å	*c*, Å	*β*, °	*V*, Å^3
$Bi_{0.15}U_{0.85}O_{2.00}$	5.463 (1)				163.04 (3)
$Bi_{0.25}U_{0.75}O_{2.00}$	5.465 (1)				163.22 (3)
$Bi_{0.32}U_{0.68}O_{2.00}$	5.467 (1)				163.40 (3)
$Bi_{0.40}U_{0.60}O_{2.00}$	5.472 (1)				163.85 (3)
$Bi_{0.50}U_{0.50}O_{2.00}$	5.478 (1)				164.35 (3)
$Bi_{0.60}U_{0.40}O_{1.95}$	5.516 (1)				167.83 (3)
$Bi_{0.67}U_{0.33}O_{2.00}$	6.889 (3)	4.007(4)	9.691 (5)	90.13 (3)	266.96 (5)
$Bi_{0.79}U_{0.21}O_{1.81}$	5.638 (1)				179.21 (3)
$Bi_{0.85}U_{0.15}O_{1.70}$	5.612 (1)				176.75 (3)

[a] The O/M ratios have been derived from the U molar fractions and XANES measurements.

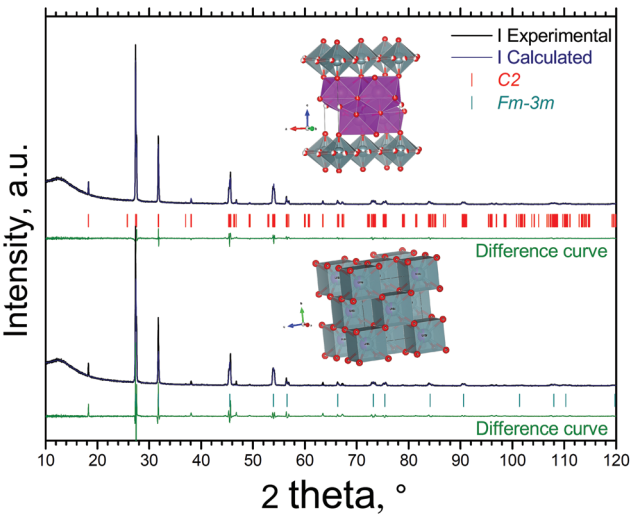

Fig. 2 Rietveld refinement of the sample $Bi_{0.67}U_{0.33}O_{2.00}$ using a monoclinic cell (S.G. *C*2) and a cubic one (S.G. $Fm\bar{3}m$). Despite a better description of the structure in the monoclinic space group, this second refinement highlights that the structure is fluorite related.

the poor quality of the refinement in $Fm\bar{3}m$ space group, the deduced lattice parameter obtained with this approach has been introduced in Fig. 1 for comparison with other compositions. Nevertheless, the monoclinic structure obtained for this composition (S.G. $C2$, a = 6.889(3) Å, b = 4.007(4) Å, c = 9.691(5) Å, β = 90.13(3)°) strongly suggest the formation of the monoclinic form of the U^{VI} compound α-Bi_2UO_6.[8–10] This hypothesis is at first quite surprising, having in mind the synthesis method (reaction of stoichiometric amounts of commercial α-Bi_2O_3 oxide and $UO_{2.10}$ at 800 °C under argon atmosphere). However, the oxidation state VI of uranium has been confirmed with XANES, as it will be presented in the next part. The source of the uranium oxidation are likely small amounts of molecular oxygen contained in the argon atmosphere.

XANES measurements. In order to investigate the oxidation states of uranium and bismuth, we performed an extensive Bi L_{III} and U L_{III} XANES and U M_{IV} HR-XANES analysis for seven selected compositions. Unfortunately, the sample with the highest bismuth content could not be measured during the U M_{IV} HR-XANES experimental campaign.

Valence state of uranium. The U M_{IV} HR-XANES spectra of different Bi–U–O compositions are presented in Fig. 3 with those of the reference samples, *i.e.* $U^{IV}O_2$, $(U^{IV},U^{V})_4O_9$, $(U^{V},U^{VI})_3O_8$ and $U^{VI}O_3$. These spectra provide unique qualitative informations on the oxidation state in the systems. The uranium oxidation states and derived molar fractions from L_{III} XANES are provided in the Table 2. These results, together with those obtained from SEM-EDS analysis, were used to calculate the oxygen content within the different Bi–U–O compositions used during this study.

As previously reported[19,20] herein we demonstrate that that the uranium oxidation states can be characterized using the U M_{IV} edge HR-XANES technique. The HR-XANES spectrum of $U^{IV}O_2$ has a pronounced peak at 3724.5 (2) eV, due to the electronic transitions from the $3d_{3/2}$ core level to the unoccupied 5f states. The $(U^{IV},U^{V})_4O_9$ HR-XANES spectrum depicts a peak at the same energy position characteristic of U^{IV} and also a peak at 3725.5 (2) eV which corresponds to U^{V}. The $(U^{V},U^{VI})_3O_8$

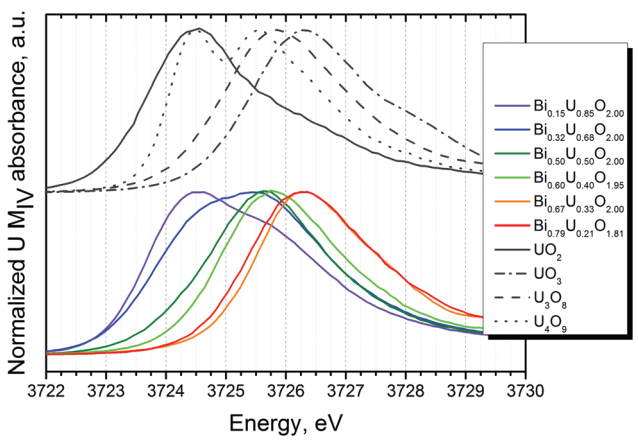

Fig. 3 U M_{IV} XANES spectra of Bi–U–O compositions.

Table 2 Uranium valence and molar fraction in the Bi–U–O compositions

Chemical composition[a]	U^{IV}	U^{V}	U^{VI}	R_f
$Bi_{0.15}U_{0.85}O_{2.00}$	82 (5)	18 (5)	0	0.005
$Bi_{0.32}U_{0.68}O_{2.00}$	44 (5)	56 (5)	0	0.020
$Bi_{0.50}U_{0.50}O_{2.00}$	0	100	0	
$Bi_{0.60}U_{0.40}O_{1.95}$	0	74 (5)	26 (5)	0.002
$Bi_{0.67}U_{0.33}O_{2.00}$	0	0	100 (5)	0.006
$Bi_{0.79}U_{0.21}O_{1.81}$	0	10 (5)	90 (5)	0.003

[a] The O/M ratios have been derived from the U molar fractions in respect of electroneutrality.

HR-XANES spectrum exhibits a white line at 3726.2 (2) eV attributed to U^{VI} and a shoulder at the lower energy side with energy position characteristic for U^{V}. The energy positions of the white line of the $U^{VI}O_3$ spectrum and the U^{VI} peak in $(U^{V},U^{VI})_3O_8$ coincide (3726.2 (2) eV) and it is characteristic for U^{VI} compounds.

Except for $Bi_{0.79}U_{0.21}O_{1.81}$, the white lines of the Bi–U–O compositions shift toward higher energy with increasing the bismuth content. This suggests an overall oxidation of uranium over the compositional range. The XANES spectra of $Bi_{0.15}U_{0.85}O_{2.00}$ and $Bi_{0.32}U_{0.68}O_{2.00}$, exhibit the two features characteristics of U^{IV} and U^{V}. However, it can be observed that the amplitude of the U^{IV} peak decreases with increasing the bismuth content.

Regarding the $Bi_{0.50}U_{0.50}O_{2.00}$ sample, its white line is a symmetric peak well aligned with the U^{V} peak of $(U^{V},U^{VI})_3O_8$. As would be expected from the electroneutrality rule, the least common factor (LCF) confirms that uranium is purely pentavalent for this composition. When increasing the bismuth content, the LCF shows that U^{VI} is progressively formed in $Bi_{0.60}U_{0.40}O_{1.95}$ and that a pure U^{VI} compound is obtained on reaching $Bi_{0.67}U_{0.33}O_{2.00}$. The formation of U^{VI} is linked to a strong increase of lattice parameter. However, the white line of $Bi_{0.79}U_{0.21}O_{1.81}$ shifts toward lower energy indicating the presence of U^{V}. This is in agreement with the lattice parameter decrease observed by XRD and Raman measurements.

Valence state of bismuth. XANES measurements at the Bi L_{III} have been performed to elucidate the bismuth valence state. The Fig. 4a and b present the Bi L_{III} XANES spectra of the Bi–U–O samples.

In the Bi L_{III} XANES spectra, there is a shift toward higher energies between the $Bi_2^{III}O_3$, $Bi_2^{III}UO_6$ and $NaBi^{V}O_3{\cdot}xH_2O$ white lines passing from Bi^{III} to Bi^{V}. Although bismuth is trivalent in both $Bi_2^{III}O_3$ and $Bi_2^{III}UO_6$, the XANES spectra are different and shifted from one another. This has already been reported[23] for other isovalent compounds and can be understood from the difference of local environment. The $NaBi^{V}O_3{\cdot}xH_2O$ spectrum exhibits a pre-edge describing $2p_{3/2}$–6s transitions corresponding to pentavalent bismuth where the 6s levels are unoccupied. This feature is not observed in our compositions, indicating that Bi remains trivalent.

The white lines of the spectra of $Bi_{0.15}U_{0.85}O_{2.00}$, $Bi_{0.32}U_{0.68}O_{2.00}$, and $Bi_{0.50}U_{0.50}O_{2.00}$ compositions have similar

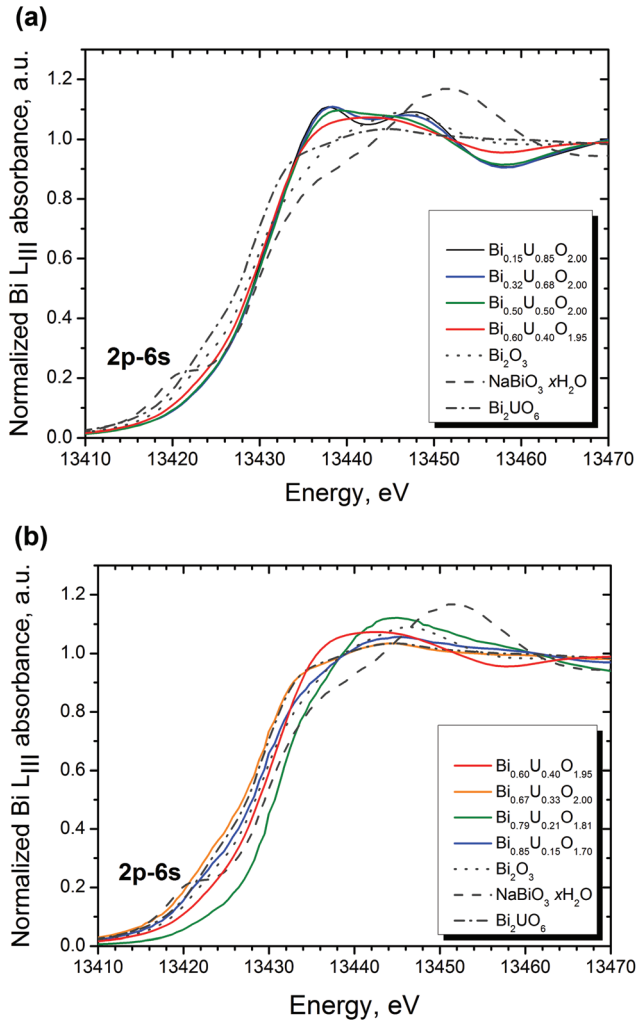

Fig. 4 (a) Bi L_{III} XANES spectra of $Bi_{0.15}U_{0.85}O_{2.00}$, $Bi_{0.32}U_{0.68}O_{2.00}$, $Bi_{0.50}U_{0.50}O_{2.00}$, and $Bi_{0.60}U_{0.40}O_{1.95}$. (b) Bi L_{III} XANES spectra of $Bi_{0.60}U_{0.40}O_{1.95}$, $Bi_{0.67}U_{0.33}O_{2.00}$, $Bi_{0.79}U_{0.21}O_{1.81}$, and $Bi_{0.85}U_{0.15}O_{1.70}$.

energy positions of their absorption edges and overall shapes. This is an indicator that the local structure of these materials is very close. However, the white lines of the remaining samples are totally different and are shifted from one another, suggesting a different local environment for each composition.

Raman spectroscopy

The Raman spectra of the samples are shown in Fig. 5. Samples with high uranium content (up to a molar ratio Bi : U = 1 : 1) reflect very poorly,[24] which explains the poor quality of their spectra (dashed black lines in Fig. 5). These spectra are compared with a spectrum from a polished surface of a pure commercial UO_2 pellet, shown in the thick bottom line in Fig. 5. Despite the noise, it can be seen that all these spectra are dominated by a band roughly centred at 445 cm^{-1}, which is assigned to the T_{2g} anti-symmetric U^{IV}–O stretching vibration typical of eight-fold coordinated uranium in the fluorite structure. It has been observed many times in UO_2 and isomorphous compounds.[25–30]

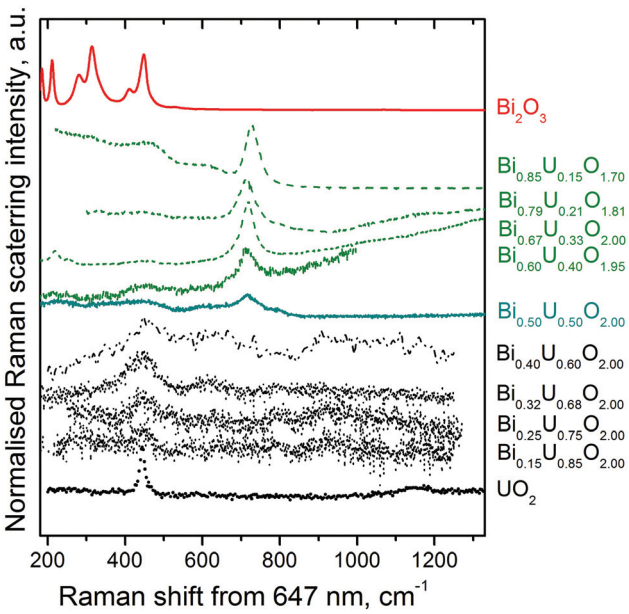

Fig. 5 Raman spectra of the Bi–U–O compositions.

Factor group theory[31] indicates that it is the only Raman active mode in the $Fm\bar{3}m$ space group. As Bi^{III} is dissolved in the UO_{2+x} lattice, this band broadens and its peak position shifts towards slightly higher energy.

Nonetheless, the fact that the T_{2g} band dominates the spectrum indicates that a fluorite structure is maintained for $Bi_{0.15}U_{0.85}O_{2.00}$, $Bi_{0.25}U_{0.75}O_{2.00}$, $Bi_{0.32}U_{0.68}O_{2.00}$, and $Bi_{0.40}U_{0.60}O_{2.00}$ compositions. The broadening of the T_{2g} mode could arise from the local disorder caused by the Bi^{III} cations in the fluorite structure. Close to the T_{2g} band, a few weak bands are observed around 570 cm^{-1} and 630 cm^{-1} which likely are linked to oxygen defects in the fluorite structure. Their presence reflects a breakdown of the translational symmetry and a reduction of the point group symmetry. Interestingly, their intensity is independent of the Bi^{III} concentration, which could suggest that doping with Bi^{III} has little effect on the oxygen sublattice and that charge compensation is then maintained by uranium atoms for compositions below $Bi_{0.50}U_{0.50}O_{2.00}$. The band at 630 cm^{-1} increases for $Bi_{0.32}U_{0.68}O_{2.00}$ and $Bi_{0.40}U_{0.60}O_{2.00}$, which is similar to observations for U_4O_9. All of these observations are in agreement with the presence of mixed valence U^{IV}/U^{V} in the material and are consistent with XANES data.

At higher bismuth content, a different spectral form is observed (presented in green in Fig. 5), reflecting a complete change of the original fluorite local symmetry, though long range order probed by XRD indicates that a fluorite organisation remains for $Bi_{0.60}U_{0.40}O_{1.95}$, $Bi_{0.79}U_{0.21}O_{1.81}$ and $Bi_{0.85}U_{0.15}O_{1.70}$. These Raman spectra, of much better quality, are largely dominated by a strong band centred around 717 cm^{-1}. The increase in the number of Raman bands indicates a decrease of local symmetry. The band at 445 cm^{-1} (T_{2g}) broadens with increasing the bismuth content together with

the appearance of weak features at low frequencies ~210 cm^{-1} and 280 cm^{-1} (typically for $Bi_{0.60}U_{0.40}O_{1.95}$ and $Bi_{0.67}U_{0.33}O_{2.00}$). These modes (at 210 cm^{-1} and 280 cm^{-1}) are also present in the Raman spectrum of Bi_2O_3, correspond to the Van Hove singularities at the gamma point of the Brillouin zone and can be assigned to Bi–O stretching vibrations. The broadening of the 445 cm^{-1} band is a consequence of an increased frequency distribution of the U–O and Bi–O vibrations, very likely due to an increased local disorder in the short range. Therefore, the assignment of this band to pure oxygen motions in a monoclinic or cubic phase is not straightforward. The XRD results suggest that this local disorder is also present in the long range for $Bi_{0.67}U_{0.33}O_{2.00}$, a monoclinic phase.

Despite the clear distortion at local range and by analogy with the Raman spectra of U_3O_8, UO_3, and UO_2^{2+} ion[32,33] the peak around 717 cm^{-1} can be attributed to a Raman active U–O stretching vibration of UO8 polyhedra with non-bonding oxygens, in close geometry to the UO_2^{2+} species. This assignment agrees well with the Raman spectrum of the hexavalent uranium compound $CaUO_4$,[34] where this vibration was clearly identified as the ν_1 stretching mode of the uranyl UO_2^{2+} ion.

Combining these observations with the XRD and XANES results, one can draw several conclusions. It can be observed, that the spectra of $Bi_{0.32}U_{0.68}O_{2.00}$ and $Bi_{0.50}U_{0.50}O_{2.00}$ displayed in Fig. 6, the T_{2g} band typical of the fluorite structure and oxygen defect bands between 570 and 630 cm^{-1}.[35] The latter lines are attributed to T_{1u} LO phonons Raman inactive in the absence of oxygen defects. They are not affected by Bi^{III} doping, suggesting that only the uranium(IV) atoms change to uranium(V) to compensate the electric charge on addition of Bi^{III}. The T_{2g} band clearly dominates the spectrum of the uranium-rich samples suggesting that the fluorite structure is maintained, whereas, in the bismuth rich region two observations can be made: (i) the band at 445 cm^{-1} broadens and its intensity reduces significantly mainly due to the increase of the local disorder at the short range distances and (ii) the dominance of the U–O stretching mode at 717 cm^{-1} suggesting formation of UO_8 species with non-bonding oxygens (similar to uranyl ions).

The spectrum of the pure U^{VI} phase $Bi_{0.67}U_{0.33}O_{2.00}$ is even more strongly dominated by this latter line in agreement with the layer organisation of α-Bi_2UO_6.

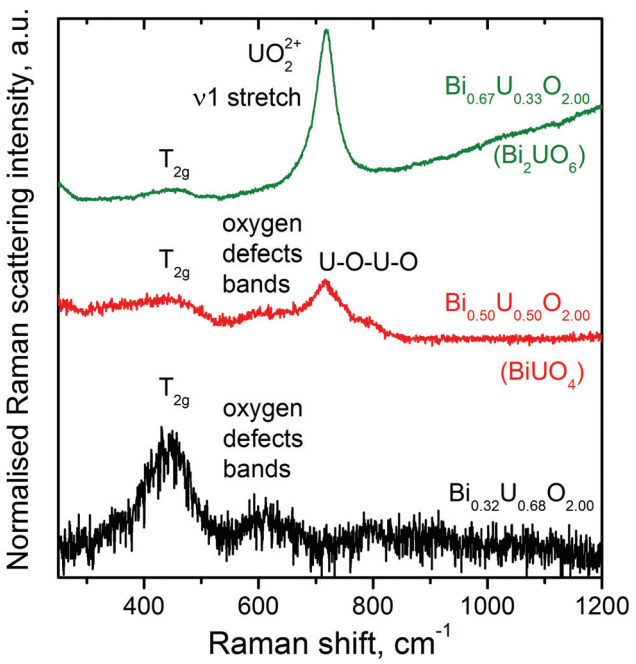

Fig. 6 Raman spectra of $Bi_{0.50}U_{0.50}O_{2.00}$, $Bi_{0.32}U_{0.68}O_{2.00}$, and $Bi_{0.67}U_{0.33}O_{2.00}$.

A special case of a U^V phase: $BiUO_4$

At 50 mol% of UO_2 and Bi_2O_3, a fluorite-type phase of general formula $U_{0.5}Bi_{0.5}O_2$ (or $BiUO_4$) forms. The cell parameter 5.478 (1) Å, is larger than UO_2 (5.471 Å). This is consistent with the average ionic radii of Bi^{III}_{CN8} (1.17 Å) and U^{V}_{CN8} (0.93 Å), with the former being slightly larger than ionic radius of U^{IV}_{CN8} = 1.00 Å. In $U_{0.5}Bi_{0.5}O_2$ the average distance M–O is 2.372 Å. The X-ray diffraction pattern with Rietveld refinement is shown in Fig. 7 and fitting results are provided in Tables 3 and 4. For oxygen atoms the displacement parameter B_{iso} is high, suggesting local disorder in agreement with the Raman observations.

The evolution of the unit-cell volume of $X^{III}UO_4$ phases as a function of eight-fold coordinated cationic radius (Fig. 8) would confirm that $BiUO_4$ belongs to this family. Note that $FeUO_4$ and $CrUO_4$, not shown in this graph, are not cubic.[36]

For some of these $X^{III}UO_4$-type compositions (X^{III} = Bi, Sc, and Y), the pentavalent oxidation state of uranium was proven based on magnetic susceptibility measurements.[13,45] This might be an indication that all the other $X^{III}UO_4$ compositions shown in this graph are pure pentavalent uranium phases.

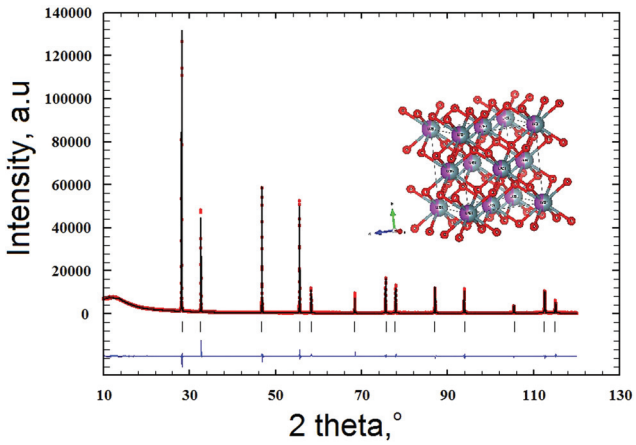

Fig. 7 Rietveld refinement of $BiUO_4$. Comparison between the observed (Y_{obs}, in red) and calculated (Y_{calc}, in black) X-ray diffraction pattern of $BiUO_4$ phase. $Y_{obs}-Y_{calc}$ (in blue) is the difference between the experimental and calculated intensities. The Bragg reflections are marked in black ticks.

Table 3 Unit cell parameters and results of the Rietveld refinement for $BiUO_4$

Formula unit	$BiUO_4$
a	5.478 (1) Å
V	164.35 Å^3
Space Group	$Fm\bar{3}m$ (N° = 225)
Z	4
Refined parameters	40
R_{wp}	7.76%
R_P	5.58%
R_B	2.08%
R_{exp}	3.83%
GOF	2.03

$R_P = \sum[y_i(obs) - y_i(calc)]/\sum y_i(obs)$; $R_{wp} = \{\sum w_i[y_i(obs) - y_i(calc)]^2/\sum y_i(obs)\}^{1/2}$. $R_B = \sum[I_{hkl}(obs) - I_{hkl}(calc)]/\sum I_{hkl}(obs)$; GOF = R_{wp}/R_{exp}.

Table 4 Atomic positions in the $BiUO_4$ compound

Atom	Oxidation state	x	y	z	B_{iso} (Å^2)
Bi	3+	0.000	0.000	0.000	0.38
U	5+	0.000	0.000	0.000	0.38
O	2−	0.250	0.250	0.250	2.89

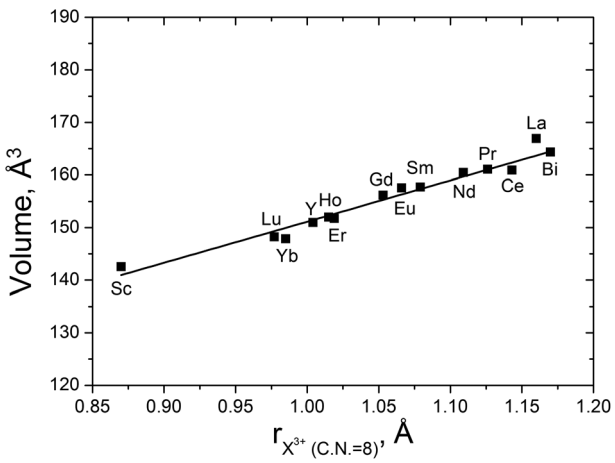

Fig. 8 Evolution of the unit-cell volume of $X^{III}UO_4$ phases as a function of eight-fold coordinated cationic radius. The unit-cell volume values are taken from the literature,[37–44] while for $BiUO_4$ the present result is shown.

Thermal expansion of $BiUO_4$ and α-Bi_2UO_6

The relative variation of the cell parameters of $BiUO_4$ and α-Bi_2UO_6 with temperature is presented in Fig. 9. The transition temperature of α-Bi_2UO_6 ($C2$ space group) to β-Bi_2UO_6 ($P\bar{3}$ space group) occurs between 600 and 800 °C, while the cubic $BiUO_4$ start to decompose into two phases above 700 °C. The expansion is more limited along the a and b directions compared to c, because of the edge-sharing of the UO_8 polyhedra (the thermal expansion along the c axis is more pronounced because of the layer structure of α-Bi_2UO_6).

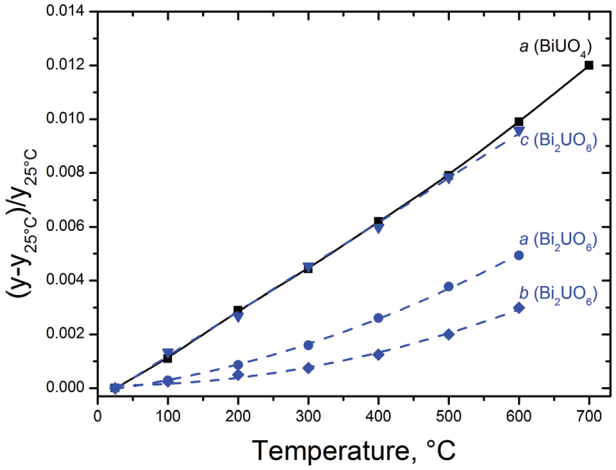

Fig. 9 Relative variation of the cell parameters of $BiUO_4$ and α-Bi_2UO_6 with temperature.

Trivalent bismuth, which is seven-fold coordinated, is poorly bonded to oxygen.

The linear thermal expansion (LTE) is defined as $LTE_{25\ °C}(T) = (x(T) - x(25\ °C))/x(25\ °C)$. The polynomial interpolation of the experimental data are presented in Fig. 9 and gives for the cubic $BiUO_4$: $LTE_{25\ °C}(T) = -3 \times 10^{-4} + 1.47 \times 10^{-5}\ T(°C) + 4.1 \times 10^{-9}\ T^2(°C)$. Similarly, the LTE for the different orientations in Bi_2UO_6 are:

a: $LTE_{25\ °C}(T) = -1 \times 10^{-4} + 3.2 \times 10^{-6}\ T(°C) + 8.8 \times 10^{-9}\ T^2(°C)$

b: $LTE_{25\ °C}(T) = 1 \times 10^{-4} - 2.0 \times 10^{-7}\ T(°C) + 8.2 \times 10^{-9}\ T^2(°C)$

c: $LTE_{25\ °C}(T) = -5 \times 10^{-4} + 1.65 \times 10^{-5}\ T(°C)$

Conclusions

The LBE cooled fast reactor concept is the basis of the MYRRHA reactor project in Belgium. As a part of the safety assessment for such reactors, detailed knowledge of potential lead and bismuth uranates/plutonates phases that could form in the event of a pin breach is needed. The present work completes our study performed in order to identify potential reaction products in the Bi–Pb–U–Pu–O system for the safety assessment for LBE cooled fast reactors.

In the current extensive investigation of the uranium(IV) oxide–bismuth(III) oxide system, the unusual behaviour of the lattice parameter variation with composition as observed by Hund[14] has been confirmed and its origin identified in the oxidation state of uranium. Even under inert atmosphere at 800 °C, U^{IV} oxidises to U^V/U^{VI} as a function of the substitution degree. We have identified the formation of the BiU^VO_4 and $Bi_2U^{VI}O_6$ compounds, within this series. All the compositions crystallise in a fluorite-related structure, but the actual symmetry of $Bi_2U^{VI}O_6$ is monoclinic. Raman spectrometry indicates changes in the local symmetry from six-fold uranium coordination to an eight-fold coordination (deduced as a func-

tion of composition) which is not observable in the long range ordering (probed by XRD). EXAFS or neutron diffraction measurements are needed in order to give more details on the local structure in those compositions.

Acknowledgements

This work was performed in the frame of the "Safe exploitation related chemistry for HLM reactors (SEARCH)" Collaborative Project (Contract Number: 295736) in the Seventh Framework Programme of the European Commission. The authors acknowledge Daniel Bouexière and Giorgio Pagliosa for room- and high-temperature X-ray diffraction measurements. We authors acknowledge the ANKA and ESRF synchrotron facilities for provision of beam time. XAS measurements have been supported by the European FP7 TALISMAN project, under contract with the European Commission.

Notes and references

1 J. Engelen, H. Aït Abderrahim, P. Baeten, D. De Bruyn and P. Leysen, *Int. J. Hydrogen Energy*, 2015, **40**, 15137–15147.
2 J. F. Vigier, K. Popa, V. Tyrpekl, S. Gardeur, D. Freis and J. Somers, *J. Nucl. Mater.*, 2015, **467**, 840–847.
3 J. G. De Jong and Ph. A. Batist, *Requeil*, 1971, **90**, 749–754.
4 H. Collette, V. Deremince-Mathieu, J. J. Verbist, Z. Gabelica, J. B. Nagy and E. G. Derouane, *J. Mol. Catal.*, 1987, **42**, 15–28.
5 J. M. Amarilla, R. M. Rojas and M. P. Herrero, *Chem. Mater.*, 1995, **7**, 341–347.
6 D. O. Charkin, D. N. Lebedev, S. Yu. Stefanovich and S. M. Kazakov, *Solid State Sci.*, 2010, **12**, 2079–2085.
7 N. L. Misra, A. K. Yadav, S. Dhara, S. K. Mishra, R. Phatak, A. K. Poswal, S. N. Jha, A. K. Sinha and D. Bhattacharyya, *Anal. Sci.*, 2013, **29**, 579–584.
8 R. N. Vannier, O. Thery, C. Kinowski, M. Huve, G. van Tendeloo, E. Suard and F. Abraham, *J. Mater. Chem.*, 1999, **9**, 435–443.
9 A. S. Kostner, J. P. P. Renaud and G. D. Rieck, *Acta Crystallogr., Sect. B: Struct. Crystallogr. Cryst. Chem.*, 1975, **31**, 127–131.
10 K. Popa, O. Beneš, P. E. Raison, J. C. Griveau, P. Pöml, E. Colineau, R. J. M. Konings and J. Somers, *J. Nucl. Mater.*, 2015, **465**, 653–656.
11 W. Rüdorff, H. Erfurth and S. Kemmler-Sack, *Z. Anorg. Allg. Chem.*, 1967, **354**, 273–238.
12 M. P. Eastman, H. G. Hecht and W. Burton Lewis, *J. Chem. Phys.*, 1971, **54**, 4141–4146.
13 C. Miyake, O. Kawasaki, K. J. Gotoh and A. Nakatani, *J. Alloys Compd.*, 1993, **200**, 187–190.
14 F. Hund, *Z. Annorg. Allg. Chem.*, 1964, **333**, 248–255.
15 J. Rothe, S. Butorin, K. Dardenne, M. A. Denecke, B. Kienzler, M. Löble, V. Metz, A. Seibert, M. Steppert, T. Vitova, C. Walther and H. Geckeis, *Rev. Sci. Instrum.*, 2012, **83**, 043105.
16 T. Vitova, M. A. Denecke, J. Göttlicher, K. Jorissen, J. J. Kas, K. Kvashnina, T. Prüßmann, J. J. Rehr and J. Rothe, *J. Phys.: Conf. Ser.*, 2013, **430**, 012117.
17 E. Kleymenov, J. van Bokhoven, C. David, P. Glatzel, J. Markus, R. Alonso-Mori, M. Studer, M. Willimann, A. Bergamaschi, B. Henrich and M. Nachtegaal, *Rev. Sci. Instrum.*, 2011, **82**, 065107.
18 B. Ravel and M. Newville, *J. Synchrotron Radiat.*, 2005, **12**, 537–541.
19 K. O. Kvashnina, S. M. Butorin, P. Martin and P. Glatzel, *Phys. Rev. Lett.*, 2013, **111**, 253002.
20 K. O. Kvashnina and F. M. F. de Groot, *J. Electron Spectrosc. Relat. Phenom.*, 2014, **194**, 88–93.
21 W. Matz, N. Schell, G. Bernhard, F. Prokert, T. Reich, J. Claußner, W. Oehme, R. Schlenk, S. Dienel, H. Funke, F. Eichhorn, M. Betyl, D. Pröhl, U. Strauch, G. Hüttig, H. Krug, W. Neumann, V. Brendler, P. Reichel, M. A. Denecke and H. Nitsche, *J. Synchrotron Radiat.*, 1999, **6**, 1076–1085.
22 J. H. Parker, Jr., D. W. Feldman and M. Ashkin, *Phys. Rev.*, 1967, **155**, 712–714.
23 S. Salem-Sugui Jr., E. E. Alp, S. M. Mini, M. Ramanathan, J. C. Campuzano, G. Jennings, M. Faiz, S. Pei, B. Dabrowski, Y. Zheng, D. R. Richards and D. G. Hinks, *Phys. Rev. B: Condens. Matter*, 1991, **43**, 5511.
24 G. M. Begun, R. G. Haire, W. R. Wilmarth and J. R. Peterson, *J. Less-Common Met.*, 1990, **162**, 129–133.
25 V. G. Keramidas and W. B. White, *J. Chem. Phys.*, 1973, **59**, 1561–1562.
26 D. Manara and B. Renker, *J. Nucl. Mater.*, 2003, **321**, 233–237.
27 T. Livneh and E. Sterer, *Phys. Rev. B: Condens. Matter*, 2006, **73**, 085118.
28 C. Jégou, R. Caraballo, S. Peuget, D. Roudil, L. Desgranges and M. Magnin, *J. Nucl. Mater.*, 2010, **405**, 235–243.
29 M. J. Sarsfield, R. J. Taylor, C. Puxley and H. M. Steele, *J. Nucl. Mater.*, 2012, **427**, 333–342.
30 R. Böhler, M. J. Welland, D. Prieur, P. Cakir, T. Vitova, T. Pruessmann, I. Pidchenko, C. Hennig, C. Guéneau, R. J. M. Konings and D. Manara, *J. Nucl. Mater.*, 2014, **448**, 330–339.
31 T. Shimanouchi, M. Tsuboi and T. Miyazawa, *J. Chem. Phys.*, 1961, **35**, 1597–1612.
32 M. L. Palacios and S. H. Taylor, *Appl. Spectrosc.*, 2000, **54**, 1372–1378.
33 F. Pointurier and O. Marie, *Spectrochim. Acta, Part B*, 2010, **65**, 797–804.
34 M. Liegeois-Duyckaerts, *Spectrochim. Acta, Part A*, 1977, **33**, 709–713.
35 L. Desgranges, G. Baldinozzi, P. Simon, G. Guimbretière and A. Canizares, *J. Raman Spectrosc.*, 2012, **43**, 455–458.
36 X. Guo, E. Tiferet, L. Qi, J. M. Solomon, A. Lanzirotti, M. Newville, M. H. Engelhard, R. K. Kukkadapu, D. Wu, E. S. Ilton, M. Asta, S. R. Sutton, H. Xu and A. Navrotsky, *Dalton Trans.*, 2016, **45**, 4622–4632.

37 F. Hund and U. Peetz, *Z. Anorg. Allg. Chem.*, 1952, **267**, 189–197.
38 F. Hund and U. Peetz, *Z. Anorg. Allg. Chem.*, 1952, **271**, 6–16.
39 F. Hund, U. Peetz and G. Kottenhahn, *Z. Anorg. Allg. Chem.*, 1955, **278**, 184–191.
40 W. Rüdorff, S. Kemmler and H. Leutner, *Angew. Chem.*, 1962, **12**, 429.
41 J. Selbin and J. D. Ortego, *Chem. Rev.*, 1968, **69**, 657–671.
42 H. Weitzel and C. Keller, *J. Solid State Chem.*, 1973, **13**, 136–141.
43 I. B. de Alleluia, M. Hoshi, W. G. Jocher and C. Keller, *J. Inorg. Nucl. Chem.*, 1981, **43**, 1831–1834.
44 Y. Hinatsu and T. Fujino, *J. Less-Common Met.*, 1989, **149**, 197–205.
45 C. Miyake, T. Isobe, Y. Yoneda and S. Imito, *Inorg. Chem. Acta*, 1987, **140**, 137–140.